Calcined layered double hydroxides/reduced graphene oxide composites with improved photocatalytic degradation of paracetamol and efficient oxidation-adsorption of As(III)

Jianyao Zhu[a], Zhiliang Zhu[a,d,*], Hua Zhang[a], Hongtao Lu[a], Wei Zhang[a], Yanling Qiu[b], Linyan Zhu[c], Stephan Küppers[c]

[a] State Key Laboratory of Pollution Control and Resource Reuse, Tongji University, Shanghai 200092, China
[b] Key Laboratory of Yangtze River Water Environment, Ministry of Education, Tongji University, Shanghai 200092, China
[c] Research Center Jülich, ZEA-3, Jülich 52425, Germany
[d] Shanghai Institute of Pollution Control and Ecological Security, Shanghai 200092, P.R. China

A B S T R A C T

The coexistence of pharmaceuticals and arsenic in natural water may exhibit a synergistic toxic effect on humans or animals. Therefore, efficient simultaneous removal of pharmaceuticals (paracetamol as a target pollutant) and arsenic from water has received increasing attention. In this study, the novel calcined ZnFe-layered double hydroxides/reduced graphene oxide (ZnFe-CLDH/RGO) composites are fabricated via a hydrothermal-calcination method. The obtained ZnFe-CLDH/RGO composites exhibit significantly improved photocatalytic performance toward degradation of paracetamol as compared to the pristine ZnFe-CLDH. The photocatalytic activity of the screened ZnFe-CLDH/RGO30 material for paracetamol degradation is about 3.5 times that of ZnFe-CLDH. The improved photocatalytic activity could be attributed to the RGO, which could lead to increased pollutant adsorption capacity and enhanced charge separation efficiency. The magnetic ZnFe-CLDH/RGO composite also shows excellent stability and reusability as a promising photocatalyst. For As(III) removal, the ZnFe-CLDH/RGO composite displays better removal efficiency in the light than in the dark. It should be ascribed to the synergy of photocatalytic oxidation of As(III) to less toxic As(V) and the accompanying arsenic adsorption. Interestingly, our study indicates that the paracetamol degradation in the mixed system of paracetamol/As(III) is more efficient than that in the single system of paracetamol. Meanwhile, arsenic can be also efficiently removed from the water samples with coexistent paracetamol and As(III) species. This work may provide a promising composite for the efficient simultaneous elimination of water environmental inorganic anions and organic pollutants.
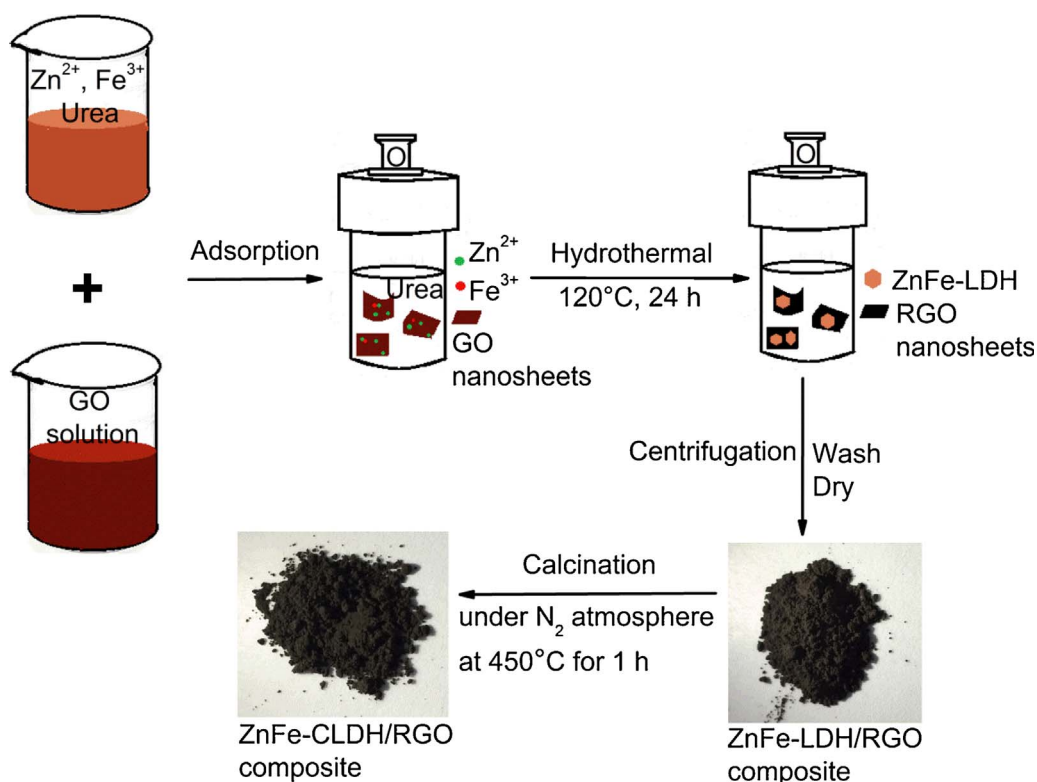
1. Introduction

Pharmaceuticals in natural water have received considerable attention in recent years as emerging contaminants. Many pharmaceuticals in aquatic environment, even at low concentration, may have an adverse effect to aquatic wildlife, ecosystem and human health [1,2]. As one of the most common medications, paracetamol is widely used in treatment of pain and fever. Because a portion of the administered dose is excreted, a substantial amount of paracetamol is released to the environment and poses potential dangers to animals and people. Its presence is likely to increase the risk of kidney cancer, liver damage and asthma [3–5]. Arsenic (As) as a kind of important inorganic contaminant in water has been of great concern throughout the world due to its hypertoxicity. Arsenic species commonly exist in the oxidation states As(III) (arsenite) and As(V) (arsenate). Inorganic trivalent form of As(III) is the most toxic among the various forms of arsenic present in natural water environment. In addition, As(III) is much more soluble and mobile than As(V), and therefore deserves more attention. The coexistence of pharmaceuticals and arsenic in natural water is a reality [6–9]. Previous studies have implied that simultaneous exposure of humans or animals to organic pollutants and arsenic may result in a synergistic toxic effect [10–12]. Therefore, efficient simultaneous removal of pharmaceuticals (such as paracetamol) and arsenic from water has received an increasing attention in recent years.

Layered double hydroxide (LDH) is a class of anionic clay consisting of positively charged brucite-like layers and negatively charged anions in the hydrated interlayer regions. LDH can be represented by this general formula, $[M_{1-x}^{II}M_x^{III}(OH)_2]^{x+}(A^{n-})_{x/n} \cdot mH_2O$, where M^{II} are

divalent cations like Mg^{2+}, Cu^{2+}, Zn^{2+}, etc., M^{III} are trivalent cations like Al^{3+}, Fe^{3+}, etc., A^{n-} denotes exchangeable interlayer anion with negative charge n, m is the number of interlayer water, and x is defined as the $M^{III}/(M^{II} + M^{III})$ ratio. LDH material is an ideal precursor to obtain various multi-metal oxides with tunable compositions after calcination treatment. The well metal dispersion can be achieved in the multi-metal oxides due to the prearrangement of metal cations in the LDH precursor. The pristine LDH and the calcined layered double hydroxide (CLDH) have been explored as photocatalysts for both organic degradation and water splitting [13–17]. On the other hand, many studies have shown that LDH and CLDH are also considered as attractive candidates for adsorption of anions [18–24].

For photocatalysis, recombination of photogenerated electrons and holes is a key barrier for high photocatalytic efficiency. Therefore, there is a great demand for a method to improve the photocatalytic efficiency by decreasing the electrons-holes recombination rate. Graphene and reduced graphene oxide (RGO) have been attracting much attention owing to their unique properties such as high electron mobility and high surface area [25–28]. During photocatalysis experiments, graphene or RGO will act both as electron-acceptor and as electron-transport materials, facilitate the migration of photogenerated electrons and hinder recombination of electrons and holes, and thus improve the photocatalytic efficiency. Several reports have pointed out that graphene or RGO could enhance the photocatalytic performance of semiconductor materials [29–33].

The objective of this study is to develop an efficient way to decontaminate the water with combined pollution of pharmaceuticals (paracetamol was selected as the target pollutant) and arsenic. Herein, the novel ZnFe-CLDH/RGO composites were designed and fabricated via a hydrothermal-calcination method. The photocatalytic activity and adsorption performance of the ZnFe-CLDH/RGO were evaluated. The magnetically separable composites exhibit improved photocatalytic degradation of paracetamol and efficient oxidation-adsorption of As(III) under light irradiation. In addition, the possible photocatalytic mechanism was also discussed in detail.

2. Experimental

2.1. ZnFe-CLDH/RGO composites preparation

Graphene oxide (GO) was provided by Nanjing Xianfeng Nano Co. (Nanjing, China). The ZnFe-CLDH/RGO composites were synthesized according to the following process (refer to Scheme 1). Appropriate GO (0, 10, 30, 50, 90 mg) was well dispersed in 50 mL of water, and the dispersion was ultrasonicated for 90 min to get GO exfoliated. Subsequently, $Zn(NO_3)_2 \cdot 6H_2O$ (3.75 mmol), $Fe(NO_3)_3 \cdot 9H_2O$ (1.25 mmol) and urea (20 mmol) were added into the GO solution. The mixture was stirred and the homogeneous mixture dispersion was sealed in a 100 mL Teflon-lined stainless steel autoclave and maintained at 120 °C for 24 h. Then the autoclave was naturally cooled to room temperature and the as-prepared sample was collected, washed with ultrapure water to remove surface impurities. After that, the product was dried at 70 °C. The samples with different initial GO weights (0, 10, 30, 50, 90 mg) were denoted as ZnFe-LDH, ZnFe-LDH/RGO10, ZnFe-LDH/RGO30, ZnFe-LDH/RGO50 and ZnFe-LDH/RGO90, respectively. The as-prepared ZnFe-LDH/RGO samples were further calcined under N_2 atmosphere at 450 °C for 1 h with a heating rate of 5 °C/min. After the heating process, the tubular furnace was naturally cooled to room temperature. The obtained materials after calcination were finally denoted as ZnFe-CLDH, ZnFe-CLDH/RGO10, ZnFe-CLDH/RGO30, ZnFe-CLDH/RGO50 and ZnFe-CLDH/RGO90, respectively.

2.2. Characterization

X-ray diffraction (XRD) patterns were measured on a D-8 Advance X-ray diffractometer (Bruker-AXS, Germany) with Cu Kα radiation operated at a voltage of 40 kV and a current of 40 mA. Thermogravimetric analysis (TGA) was performed using a TA Instruments Q600 SDT thermal analyzer (USA) under air. The samples were heated from 50 °C to 900 °C at a rate of 10 °C/min. Fourier transform infrared (FTIR) spectra were recorded in the range 4000–400 cm^{-1} on a Nicolet 5700 FTIR spectrometer (Thermo Nicolet,
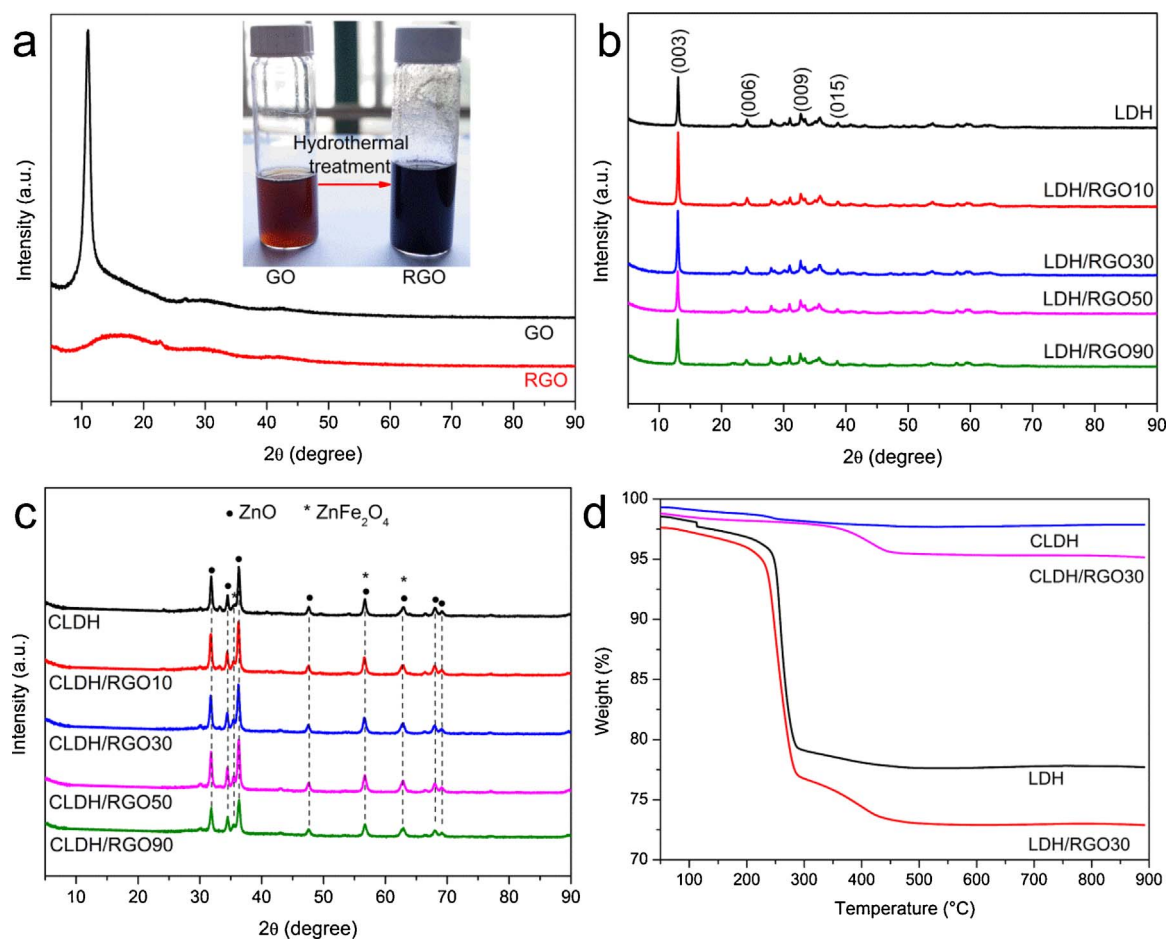
Fig. 1. (a) XRD patterns of GO and RGO (inset is the color change of GO after hydrothermal treatment); (b) XRD patterns of ZnFe-LDH and ZnFe-LDH/RGO with different RGO contents; (c) XRD patterns of ZnFe-CLDH and ZnFe-CLDH/RGO with different RGO contents; (d) Thermogravimetric analysis curves of ZnFe-LDH, ZnFe-LDH/RGO30, ZnFe-CLDH and ZnFe-CLDH/RGO30.

USA). Raman spectra were obtained on a Raman micro spectrometer (Renishaw Crop., UK) using a semiconductor laser at a wavelength of 532 nm. The morphologies and structures were characterized with a field-emission scanning electron microscope (SEM, Hitachi S-4800, Japan) and a transmission electron microscope (TEM, JEM-2011, JEOL, Japan). The Brunauer-Emmett-Teller (BET) surface area was measured by nitrogen adsorption/desorption isotherms at 77 K using an Autosorb-iQ analyzer (Quantachrome, USA). The zeta potential was determined with a Zetasizer Nano ZS90 (Malvern, UK). The magnetic property was measured on a Quantum Design PPMS DynaCool system (USA) at room temperature (300 K). UV–vis diffuse reflectance spectra (DRS) of photocatalysts were recorded on a Shimadzu UV-2550 spectrophotometer (Japan) equipped with an integrating sphere using $BaSO_4$ as a reference. Photoluminescence (PL) spectra of the samples were recorded with a FluoroMax-4 spectrofluorometer (Horiba, Japan) by using the excited wavelength of 310 nm. X-ray photoelectron spectroscopy (XPS) analysis was conducted on a Thermo Fisher Scientific ESCALAB 250Xi photoelectron spectrometer (USA) with Al Kα radiation ($h\nu$ = 1253.6 eV).

The photocurrent and electrochemical impedance were measured in a standard three-electrode system on a CHI660C electrochemical workstation (Chenhua, China) by using 0.5 M Na_2SO_4 electrolyte. The irradiation area was 1 cm^2 under a 300 W xenon lamp. A Pt foil electrode as the counter electrode, an Ag/AgCl electrode as the reference electrode and an indium tin oxide (ITO) glass covered with the photocatalyst as the working electrode. The working electrodes were prepared as follows: 0.18 g of the as-prepared sample and 0.02 g polyvinylidene fluoride (PVDF) were dispersed in N-methyl pyrrolidone.

Then the slurry was put evenly on the conductive side of the ITO glass and dried in an oven at 60 °C.

2.3. Photocatalysis and adsorption experiments

The experiments for paracetamol degradation or/and As(III) oxidation-adsorption were performed under simulated solar light irradiation. The simulated solar light irradiation was provided by a 500 W xenon lamp with a 300 nm cut-off filter (NBeT, China), which was positioned in the cylindrical quartz cold trap. The system was cooled by circulating water and maintained at room temperature. The desired 25 mg of powdered sample was added into 50 mL paracetamol solution (5 mg/L) or/and As(III) solution (1 mg/L). The distance between the light source and the surface of the reaction solution is 8 cm. During the experiments, aliquots of the reaction solution were sampled at given time intervals and filtered to remove the solid samples. For paracetamol degradation, the solutions were magnetically stirred in the dark for 30 min to reach adsorption equilibrium of paracetamol on the photocatalysts before the irradiation. Adsorption experiments of paracetamol/arsenic were carried out following the same procedure of photocatalytic tests but in the dark. The concentration of paracetamol was determined on a Waters Acquity ultra-performance liquid chromatography I-class system equipped with a photodiode array detector (UPLC-PDA, USA). The arsenic was analyzed on an atomic fluorescence spectrometer (AFS, Pgeneral, China). Total organic carbon (TOC) measurements were accomplished with a TOC analyzer (TOC-L, Shimadzu, Japan).
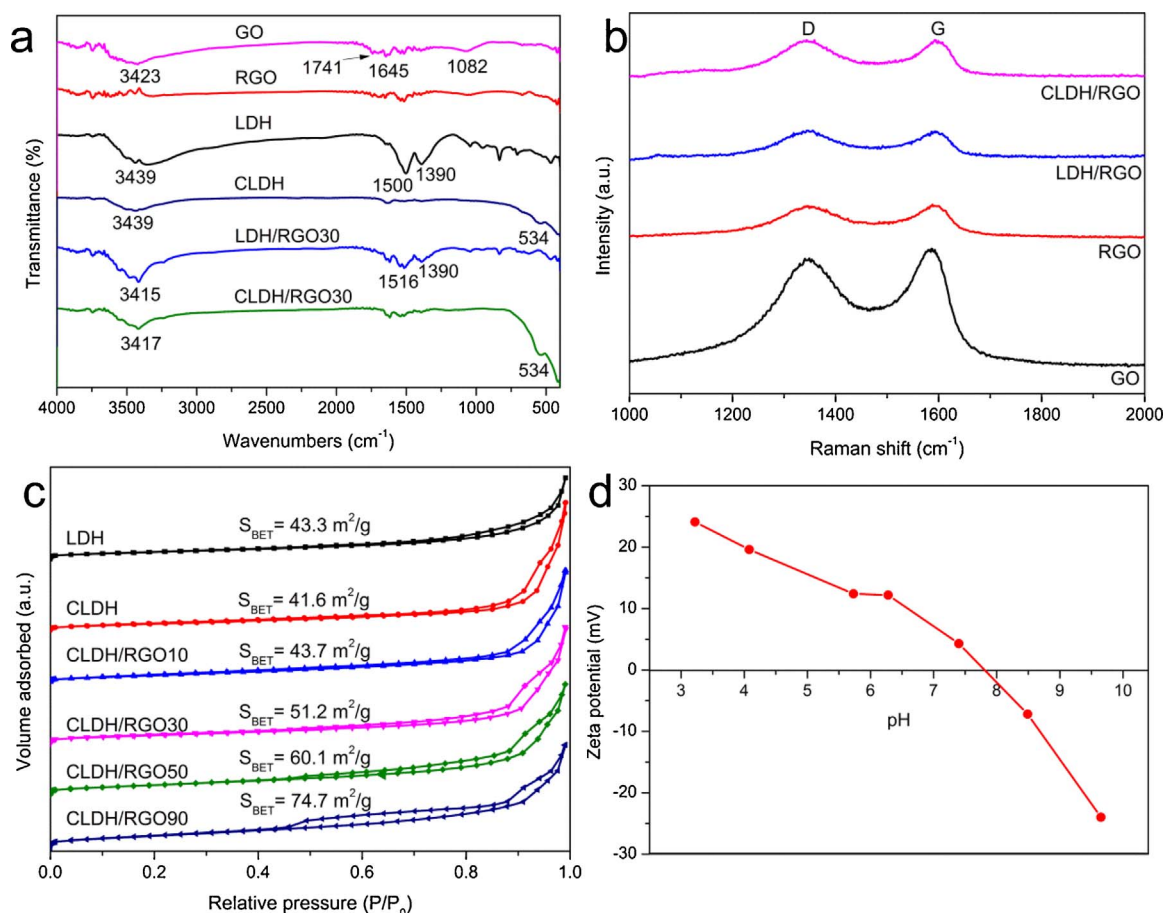
Fig. 2. (a) FTIR spectra of GO, RGO, ZnFe-LDH, ZnFe-CLDH, ZnFe-LDH/RGO30 and ZnFe-CLDH/RGO30; (b) Raman spectra of GO, RGO, ZnFe-LDH/RGO30 and ZnFe-CLDH/RGO30; (c) N$_2$ adsorption-desorption isotherms of ZnFe-LDH and ZnFe-CLDH/RGO with different RGO contents; (d) Zeta potentials of ZnFe-CLDH/RGO30 as a function of pH.
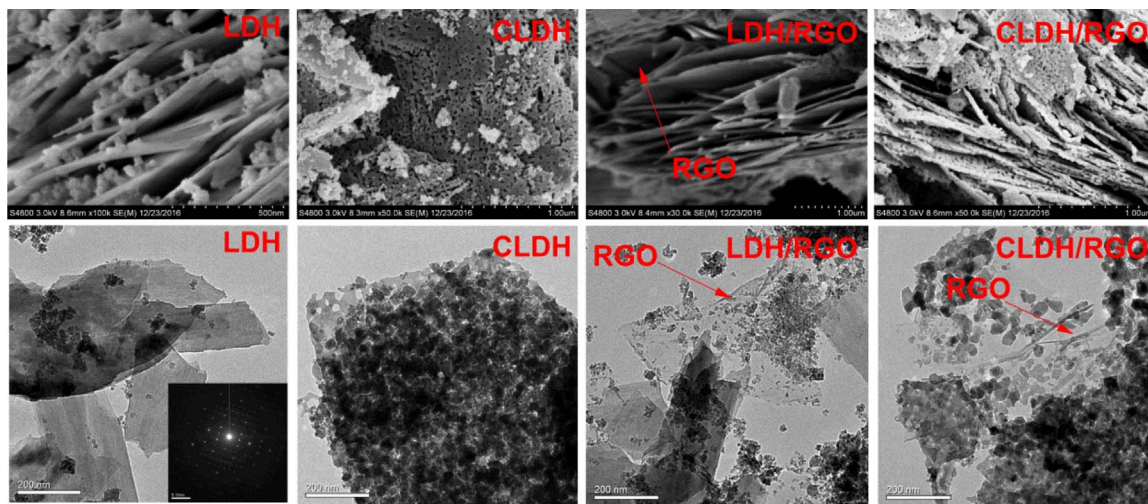

Fig. 3. SEM and TEM images of ZnFe-LDH, ZnFe-CLDH, ZnFe-LDH/RGO30 and ZnFe-CLDH/RGO30. Inset is the SAED pattern of ZnFe-LDH.

3. Results and discussion

3.1. Characterization of as-prepared samples

The XRD pattern of GO shows a sharp and strong diffraction peak at $2\theta = 11.0°$ (Fig. 1a), corresponding to a d-spacing value of 0.80 nm. This result is in agreement with the lamellar structure of GO. However, for the RGO obtained from the hydrothermal treatment, the XRD pattern of RGO displays an amorphous structure. This result indicates that

either all stacking of graphene layers in RGO is lost, or any remaining stacking is disordered [34]. In addition, it can clearly be seen from Fig. 1a (inset) that the color of GO dispersion changed from wine red to black after hydrothermal treatment. These results suggest that GO can be reduced to RGO without added reducing agent via hydrothermal treatment. Fig. 1b shows the XRD patterns of the prepared ZnFe-LDH and ZnFe-LDH/RGO with different RGO contents. The XRD pattern of ZnFe-LDH is consistent with the previous report [15]. The diffraction peaks of (003) ($2\theta = 13.0°$) is especially strong, while other peaks have
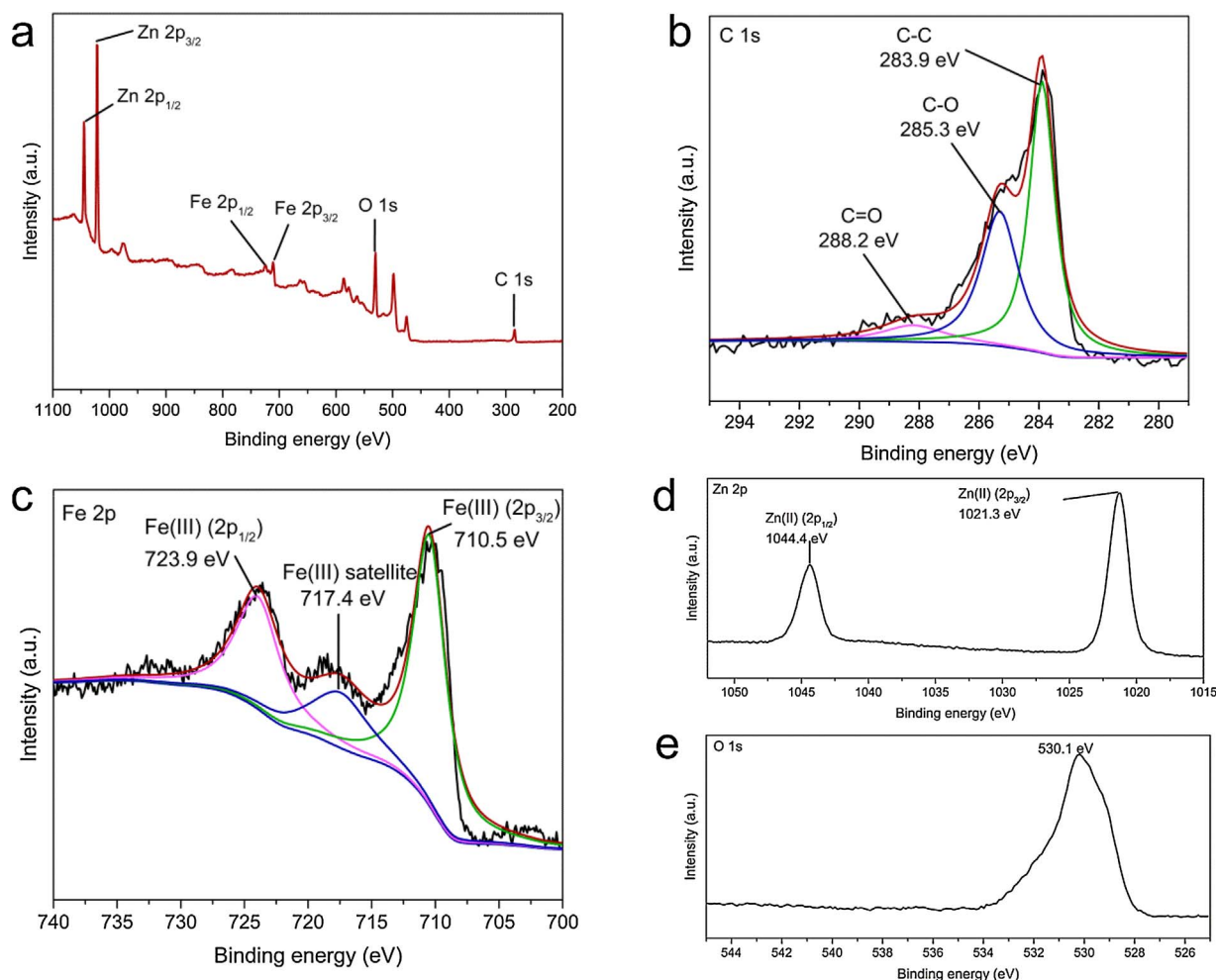
Fig. 4. (a) Full XPS spectrum of ZnFe-CLDH/RGO30 and the high resolution XPS spectra of (b) C 1s, (c) Fe 2p, (d) Zn 2p and (e) O 1s.

relatively weak intensities, suggesting that the crystal grew along a certain axis. It is observed that the ZnFe-LDH/RGO composites with different RGO contents exhibit similar XRD patterns, which are the same as that of ZnFe-LDH. The results indicate that the RGO loading does not destroy the layered structure of LDH. The XRD patterns of the ZnFe-CLDH and ZnFe-CLDH/RGO with different RGO contents are given in Fig. 1c. It can be easily observed that the structure of LDH material was destroyed and the characteristic diffraction peaks of ZnO phase and $ZnFe_2O_4$ spinel phase appeared after calcination treatment. The XRD peaks of ZnO phase in the present study are consistent with that observed in the ZnAl-CLDH sample reported by our previous study [14].

TGA is an effective analytical approach to evaluate the content of RGO in samples. As shown in Fig. 1d, the TGA curves of ZnFe-LDH and ZnFe-LDH/RGO30 have two distinct weight losses in the temperature ranges of 50–285 °C, 285–470 °C. For the TGA curve of ZnFe-LDH, the weight loss is related to the loss of water, the dehydroxylation of the LDH sheets and the removal of carbonates from the interlayer [35]. In addition, the weight loss of ZnFe-LDH/RGO30 also includes the decomposition of RGO. In the temperature range of 470–900° C, there is almost no weight loss, implying the RGO is entirely decomposed. For ZnFe-CLDH and ZnFe-CLDH/RGO30, the weight losses are not obvious. According to the TGA results, the contents of RGO in ZnFe-LDH/RGO30 and ZnFe-CLDH/RGO30 are 5.31 wt% and 2.25 wt%, respectively.

Fig. 2a shows the FTIR spectra of as-prepared samples in the range 4000–400 cm^{-1}. GO exhibits a series of oxygen containing groups, the broad band at around 3423 cm^{-1} is due to the O−H stretching vibration, the band at 1741 cm^{-1} reflects the carbonyl C=O vibration, the

band at 1082 cm^{-1} can be assigned to alkoxy C−O stretching vibration [36,37]. In addition, the band at 1645 cm^{-1} is attributed to skeletal vibration [37]. In comparison to the FTIR spectrum of GO, the bands at 3423 cm^{-1}, 1741 cm^{-1} and 1082 cm^{-1} of RGO almost disappeared or reduced significantly, indicating that GO has been reduced to a great extent. The FTIR spectra of ZnFe-LDH and ZnFe-LDH/RGO30 are very similar. The broad band at around 3439 cm^{-1} can be assigned to the stretching vibration of the O−H bond of the hydroxyl groups and H_2O molecules. The appearance of band at 1390 cm^{-1} is the ν_3 (asymmetric stretching) of CO_3^{2-} in the interlayer, suggesting that some CO_3^{2-} exist in the gallery of LDH sample. Furthermore, the bands in the range of 400–800 cm^{-1} can be interpreted as lattice vibration modes of M-OH and M-O. It is noteworthy that a band around 1500 cm^{-1} for LDH is observed, which can be ascribed to adsorbed CO_3^{2-} species [38]. As shown in Fig. 2a, ZnFe-CLDH and ZnFe-CLDH/RGO30 also display similar FTIR spectra. Compared with the LDH, the broad band intensity at around 3439 cm^{-1} is lower, revealing that H_2O molecules were continuously removed from the LDH during the calcination. The bands of CLDH at around 1500 cm^{-1} and 1390 cm^{-1} almost disappear because of the decomposition of CO_3^{2-} groups. Moreover, the band observed near 534 cm^{-1} could be attributed to the vibration of the M-O bond. The O−H bond band position 3415–3439 cm^{-1} possesses lower wave number for LDH/RGO and CLDH/RGO compared to that for LDH and CLDH, which can be ascribed to the effective combination of LDH and RGO.

Raman spectroscopy is a non-destructive method to characterize carbon-based materials. Fig. 2b shows the Raman spectra of GO, RGO, ZnFe-LDH/RGO and ZnFe-CLDH/RGO. All four display a D band at
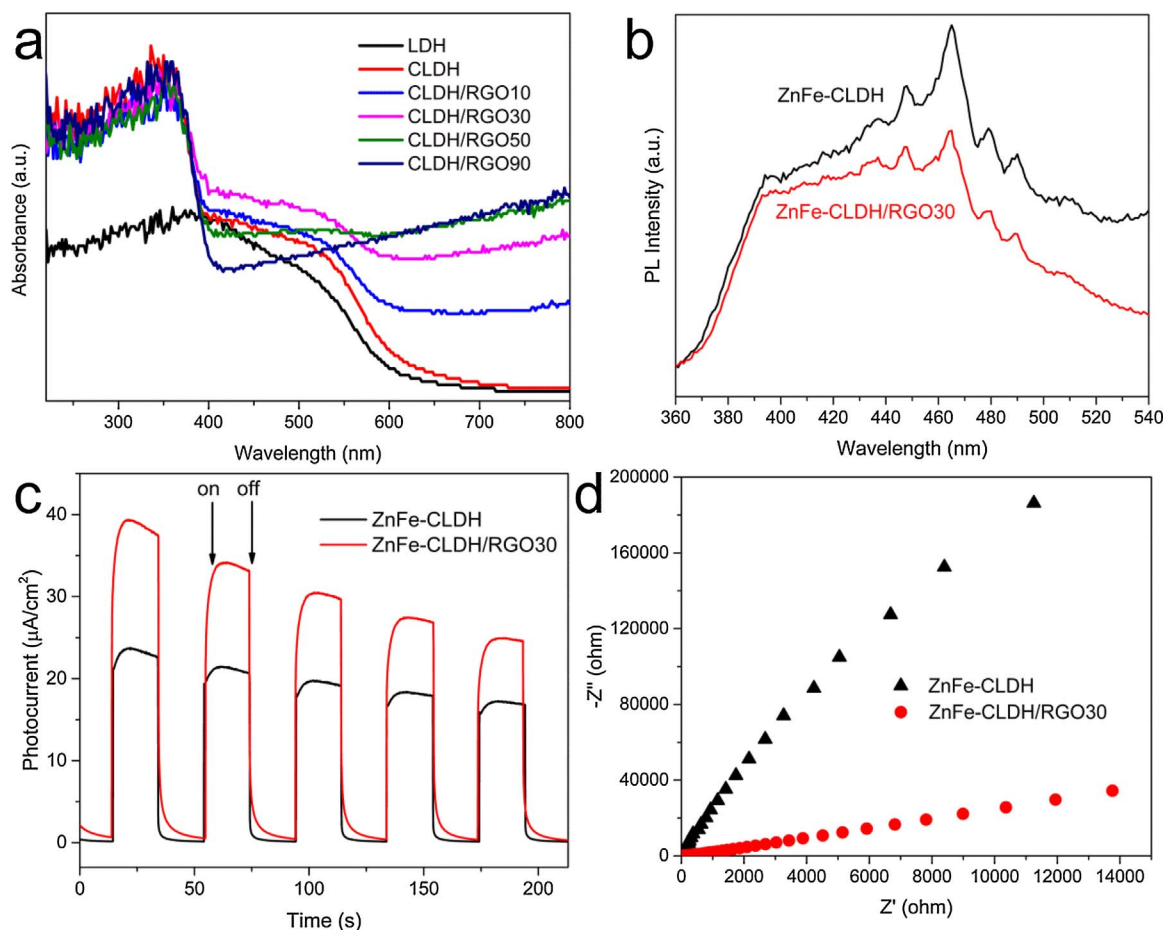
Fig. 5. (a) The UV–vis diffuses reflectance spectra of ZnFe-LDH and ZnFe-CLDH/RGO with different RGO contents; (b) PL spectra of ZnFe-CLDH and ZnFe-CLDH/RGO30; (c) Transient photocurrent density versus time plotted for ZnFe-CLDH and ZnFe-CLDH/RGO30 under simulated solar light irradiation; (d) EIS Nyquist plots of ZnFe-CLDH and ZnFe-CLDH/RGO30.

~1346 cm^{-1} corresponding to structural defects and a G band at ~1588 cm^{-1} related to the first-order scattering of the E_{2g} mode observed for sp^2-carbon domains [39,40]. In general, the intensity ratio of D and G bands (I_D/I_G) is a measure of the relative concentration of local defects/disorders and average size of the sp^2 domains in graphite materials. Compared with GO ($I_D/I_G = 0.929$), an increased I_D/I_G intensity ratio for the RGO ($I_D/I_G = 0.961$), LDH/RGO ($I_D/I_G = 1.016$) and CLDH/RGO ($I_D/I_G = 0.997$) is observed, indicating that the reduction process increases the defect content or edge area in RGO sheets [39]. In addition, it is reasonable to consider that the reduction of GO causes fragmentation along the reactive sites and produces new graphitic domains, which leads to smaller RGO but more in numbers [41]. As a result, the small size of RGO results in a large quantity of edges. The edges act as defects to result in the increase in the D band [42].

Fig. 2c displays the N$_2$ adsorption-desorption isotherms of ZnFe-LDH and ZnFe-CLDH/RGO with different RGO contents. The adsorption-desorption isotherms of all samples exhibit the characteristics of types IV isotherms with a H3 type hysteresis loop in the IUPAC classification. The H3 type hysteresis loop is related to slit-shaped pores of packing plate-like particles. We can observe from Fig. 2c that all the CLDH/RGO composites have higher BET surface area than CLDH, and the BET surface area increases with increasing RGO content. It should be attributed to the high BET surface area of RGO. In general, higher surface area can provide more active sites for paracetamol adsorption. The results are consistent with the paracetamol adsorption experimental results (Fig. 6b).

The zeta potential of ZnFe-CLDH/RGO30 composite was measured to confirm the surface charge property (Fig. 2d). The pH at point of zero charge (pH$_{pzc}$) of the ZnFe-CLDH/RGO30 composite is 7.8.

The morphologies and structures of the ZnFe-LDH, ZnFe-CLDH, ZnFe-LDH/RGO30 and ZnFe-CLDH/RGO30 were characterized by SEM and TEM, as shown in Fig. 3. It can be seen that the ZnFe-LDH and ZnFe-LDH/RGO30 show plate-like structure, which is typical for the LDH morphology. The structure of ZnFe-LDH was further characterized by selected area electron diffraction (SAED). The SAED pattern reveals the crystalline nature of ZnFe-LDH. When the ZnFe-LDH and ZnFe-LDH/RGO30 were calcined at 450 °C for 1 h, the oxides crystallization occurred. However, the lamellae of samples were not completely broken and covered with small holes. The RGO can be observed from the electron microscopy images of both ZnFe-LDH/RGO30 and ZnFe-CLDH/RGO30 and the RGO exhibits a typical wrinkled texture.

XPS was used to measure and examine the chemical composition of the ZnFe-CLDH/RGO30. As shown in Fig. 4a, the survey XPS spectrum suggests the presence of Zn, Fe, O and C. The high resolution XPS spectrum of C 1 s is shown in Fig. 4b. It can be deconvoluted into three components with binding energies at about 283.9, 285.3 and 288.2 eV, attributable to C−C, C−O and C=O species, respectively [43,44]. In the Fe 2p high resolution XPS spectrum (Fig. 4c), two distinct peaks appear at binding energies of 710.5 eV for Fe 2p$_{3/2}$ and 723.9 eV for Fe 2p$_{1/2}$, with a small satellite peak between them, which is characteristic of Fe^{3+} [45]. The peaks at 1044.4 and 1021.3 eV can be ascribed to Zn 2p$_{1/2}$ and Zn 2p$_{3/2}$ of Zn^{2+}. The O 1 s peak can be found at 530.1 eV, which is characteristic of oxygen in metal oxides.

Fig. 5a shows the UV–vis DRS of the photocatalysts, which reflect the optical properties of the materials in different wavelength ranges. It can be seen that the introduction of different weight contents of RGO has a significant effect on the light absorption property for the ZnFe-CLDH/RGO. The absorbance in the visible light region ranging from
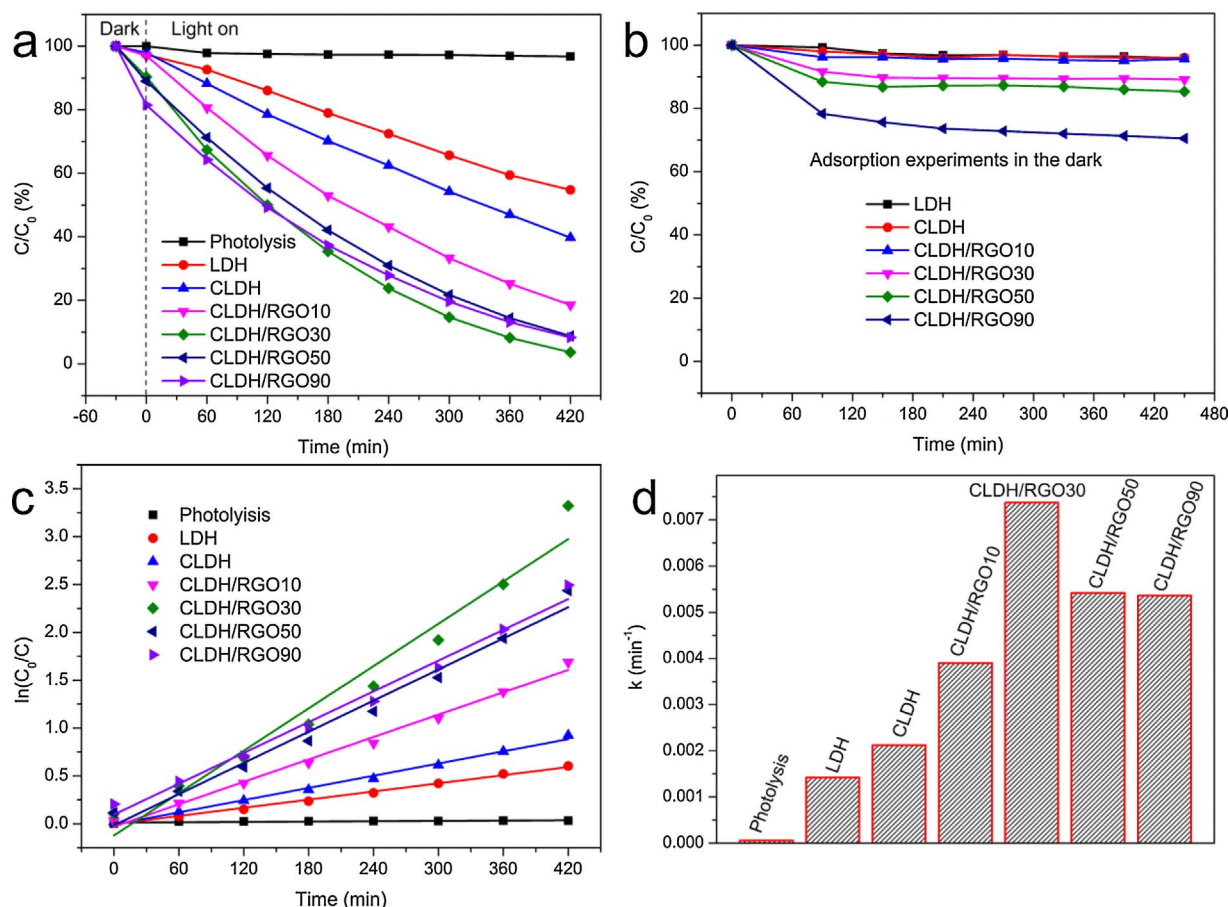
Fig. 6. (a) Photocatalytic degradation of paracetamol by ZnFe-LDH and ZnFe-CLDH/RGO with different RGO contents; (b) Adsorption of paracetamol by ZnFe-LDH and ZnFe-CLDH/RGO with different RGO contents; (c) Pseudo-first-order kinetic plot for the photocatalytic degradation of paracetamol by ZnFe-LDH and ZnFe-CLDH/RGO with different RGO contents; (d) Photocatalytic degradation rate constants of ZnFe-LDH and ZnFe-CLDH/RGO with different RGO contents. Photolysis represents the test withoutphotocatalyst.

400 to 600 nm increases first and then decreases with the increased RGO content. In range from 600 to 800 nm, the absorbance increases with the increased RGO content. Nevertheless, the optical absorption edge of ZnFe-CLDH/RGO is similar to that of ZnFe-CLDH. Compared with the ZnFe-LDH, the ZnFe-CLDH exhibits stronger absorbance, especially below 400 nm.

The PL spectra were employed to investigate the combination and separation of the photogenerated carriers. Generally speaking, a higher PL intensity represents a higher recombination rate and a lower PL intensity expresses a lower recombination rate. As presented in Fig. 5b, ZnFe-CLDH/RGO30 nanocomposite shows a lower PL intensity than ZnFe-CLDH, indicating that RGO contributes to decreasing the recombination of electron-hole pairs and enhancing the charge separation efficiency.

The charge separation and migration could notably affect the photocatalytic performance, which could be confirmed by the photocurrent response. Fig. 5c shows the transient photocurrent responses of ZnFe-CLDH and ZnFe-CLDH/RGO30 with 20 s light on/off cycles. The photocurrent for ZnFe-CLDH/RGO30 nanocomposite exhibits a significant enhancement compared to ZnFe-CLDH, which indicates that the introduction of RGO into ZnFe-CLDH effectively inhibits the recombination of electron-hole pairs.

In order to evaluate the kinetics of charge transfer in ZnFe-CLDH and ZnFe-CLDH/RGO30, electrochemical impedance spectroscopy (EIS) measurements were performed. The diameter of semicircle in the Nyquist plots in EIS measurements is considered to relate to the charge transfer resistance and a smaller arc radius represents higher efficiency in charge transfer [46]. As shown in Fig. 5d, ZnFe-CLDH/RGO30 displays a smaller arc radius in the EIS Nyquist plot than ZnFe-CLDH. This

result suggests that ZnFe-CLDH/RGO30 displays a preferable efficiency of charge transfer.

3.2. Photocatalytic degradation of paracetamol

The photocatalytic activities of the ZnFe-LDH and ZnFe-CLDH/RGO with different RGO contents were evaluated by the photodegradation of paracetamol under simulated solar light irradiation (Fig. 6a). Paracetamol is extremely poorly degraded by the direct photolysis (without photocatalyst), indicating that the pollutant is relatively stable and the self-photolysis process can be ignored. As shown in Fig. 6a, the photocatalytic activity increases after calcination treatment at 450°C for 60 min. It can be attributed to the formation of highly photocatalytically active multi-metal oxides during the calcination, as shown by the XRD spectrum of the ZnFe-CLDH (Fig. 1c).

The amount of the RGO in the composite greatly affects the photocatalytic performance. On the basis of photodegradation rates, all of ZnFe-CLDH/RGO samples exhibit enhanced photocatalytic decomposition compared with ZnFe-CLDH alone. The photocatalytic activity increases with increasing RGO content. The improved photocatalytic performance should be mainly due to the increased pollutant adsorption capacity (Fig. 6b) and enhanced charge separation efficiency. However, further increase of RGO content decreases the photocatalytic activity of the catalyst. Although higher content of RGO can adsorb large quantities of pollutants, it can limit the contact surface of ZnFe-CLDH with the light leading to lower photocatalytic activity. As a consequence, a suitable content of RGO is crucial for optimizing the photocatalytic activity of ZnFe-CLDH/RGO composites. The overall photocatalytic efficiency is in the order ZnFe-LDH < ZnFe-CLDH <
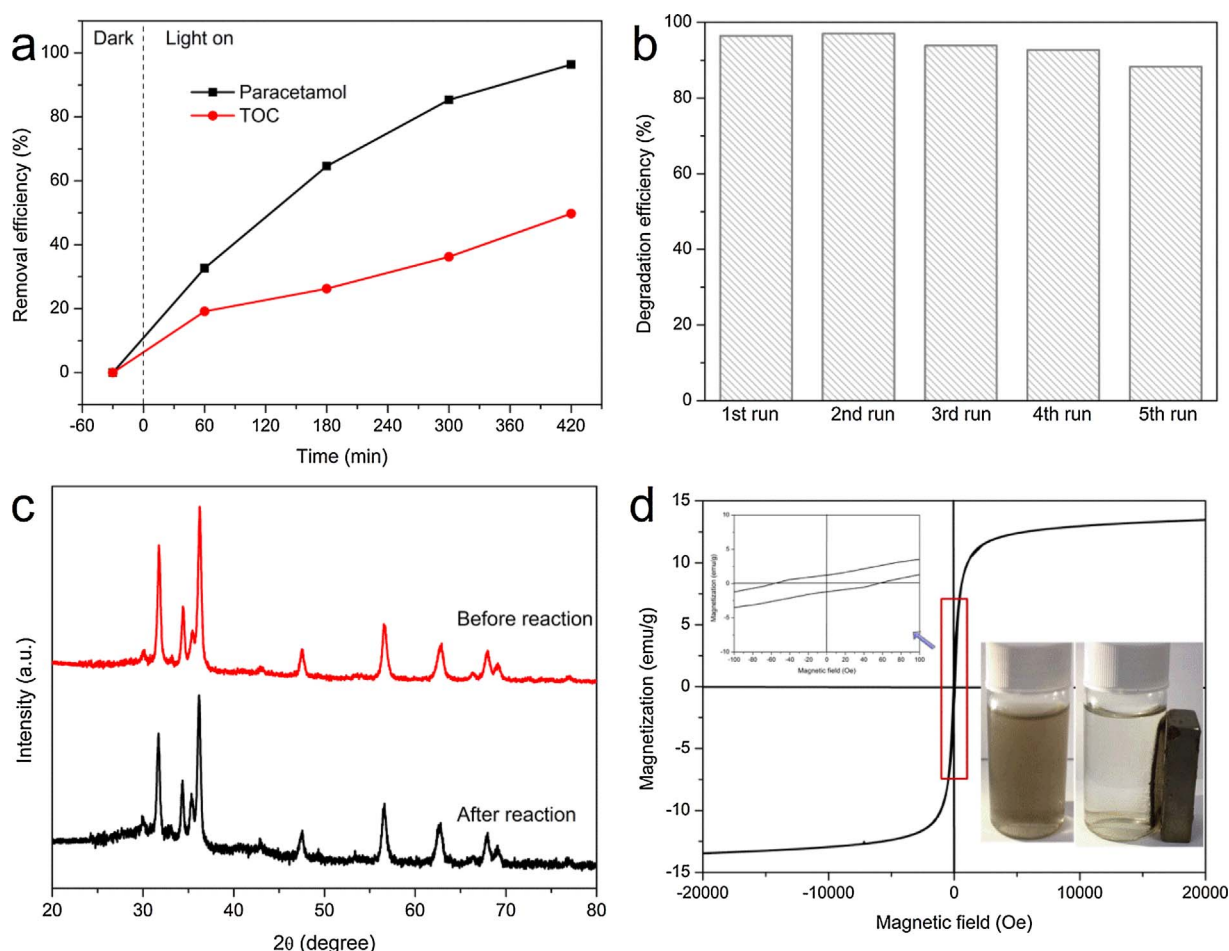
Fig. 7. (a) The paracetamol and TOC removal efficiency during the course of the photocatalytic degradation with ZnFe-CLDH/RGO30 composite; (b) Cycling runs for the photocatalytic degradation of paracetamol in the presence of ZnFe-CLDH/RGO30; (c) XRD patterns of the ZnFe-CLDH/RGO30 before and after the cycling photocatalytic reaction; (d) Room-temperature hysteresis loop of ZnFe-CLDH/RGO30, Inset: Photographs of the ZnFe-CLDH/RGO30 suspended in the aqueous solution quickly response to a magnet.

ZnFe-CLDH/RGO10 < ZnFe-CLDH/RGO90 ≈ ZnFe-CLDH/RGO50 < ZnFe-CLDH/RGO30. As can be seen from Fig. 6a, at least 95% of paracetamol can be degraded by ZnFe-CLDH/RGO30 over the period of 420 min, concluding that the ZnFe-CLDH/RGO30 exhibits the highest synergistic effect between ZnFe-CLDH and RGO.

To quantitatively understand the reaction kinetics of the paracetamol degradation, a pseudo-first-order reaction kinetic model was used and expressed by the following equation:

$$\ln\left(\frac{C_0}{C}\right) = k_{app}t$$

where k_{app} (min^{-1}) is the apparent rate constant and t (min) is the time of irradiation. C_0 (mg/L) and C (mg/L) are paracetamol concentrations of the solution at time 0 and t, respectively. The corresponding linear transforms in $ln(C_0/C)$ as a function of irradiation time are given in Fig. 6c. From the figure, we can get the apparent rate constants of the photocatalysts. The obtained values are shown in Fig. 6d. The results clearly reveal that ZnFe-CLDH/RGO30 exhibits the highest photocatalytic activity with an apparent rate constant k_{app} = 0.00737 min^{-1}, which is about 3.5 times that of ZnFe-CLDH (0.00212 min^{-1}). These results indicate that the photocatalytic activity of ZnFe-CLDH can be obviously improved in the presence of RGO.

TOC is widely used to evaluate the degree of mineralization of organic pollutants. As shown in Fig. 7a, TOC was measured in the photocatalytic degradation process by the ZnFe-CLDH/RGO30 composite under light irradiation. It is observed that the TOC removal is much slower than the degradation of paracetamol. After 420 min, the removal

efficiency of paracetamol reaches 96.4% while the mineralization degree is only 49.8%. The result implies that a longer time of photocatalysis is required to obtain complete mineralization.

For the practical applications, stability and reusability of photocatalysts are greatly important. The cycling experiment was performed with ZnFe-CLDH/RGO30. The photocatalyst dose and the paracetamol concentration used in the experiment were 0.5 g/L and 5 mg/L (50 mL), respectively. After simulated solar light irradiation for 420 min, the photocatalyst was recovered and re-dispersed in paracetamol solution for the next run. It is observed that the degradation efficiency of ZnFe-CLDH/RGO30 for paracetamol with a slight decrement of 8.1% after five successive experimental runs (Fig. 7b). The decrease on the photocatalytic activity during the repeated runs is partly ascribed to the loss of the photocatalyst. Fig. 7c exhibits the XRD patterns of ZnFe-CLDH/RGO30 before and after the cycling photocatalytic reaction. After five consecutive photocatalysis runs, the crystalline structure is still well preserved. In addition, measurement of magnetization versus applied field for ZnFe-CLDH/RGO30 is plotted in Fig. 7d. The saturation magnetization (Ms), coercivity (Hc) and retentivity (Mr) of ZnFe-CLDH/RGO30 are 13.5 emu/g, 53.9 Oe and 1.23 emu/g, respectively. The as-prepared ZnFe-CLDH/RGO30, suspended in the aqueous solution, can quickly respond to a magnet (Fig. 7d, inset) and thus can be easily separated and recovered by an external magnet. These results elucidate the excellent stability and reusability of ZnFe-CLDH/RGO as a promising photocatalyst for water purification.

To unveil the mechanism for the photocatalytic degradation of paracetamol over ZnFe-CLDH/RGO, we carried out trapping
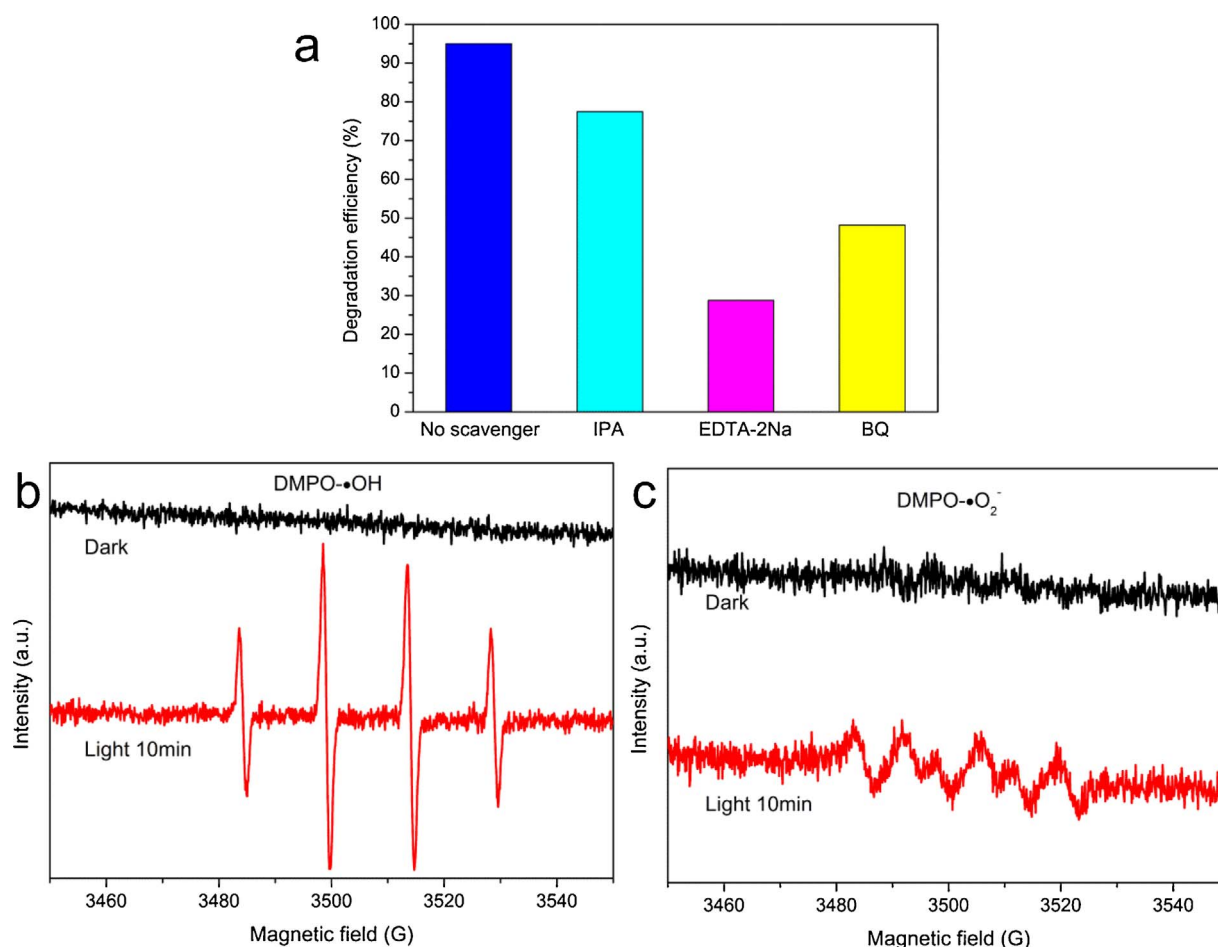
Fig. 8. (a) Effects of different scavengers on the degradation of paracetamol by ZnFe-CLDH/RGO30 under simulated solar light irradiation; DMPO spin-trapping EPR spectra of ZnFe-CLDH/RGO30 in aqueous dispersion for DMPO-·OH (b) and in methanol dispersion for DMPO-·O_2^- (c) before and after 10 min under simulated solar light irradiation.

experiments of active species such as superoxide radical (·O_2^-), hole (h$^+$) and hydroxyl radical (·OH) in photocatalytic process. Herein, 0.5 mmol/L p-benzoquinone (BQ), 0.5 mmol/L ethylenediamine tetra-acetic acid disodium salt (EDTA-2Na) and 0.5 mmol/L isopropyl alcohol (IPA) were employed as the scavengers of ·O_2^-, h$^+$ and ·OH, respectively [14]. As shown in Fig. 8a, the photocatalytic degradation efficiency of paracetamol was significantly depressed when EDTA-2Na was used as an h$^+$ scavenger. Obvious change in the degradation efficiency of paracetamol is also observed upon the addition of BQ as a ·O_2^- scavenger as compared to the no scavenger experiment under same condition. Moreover, when IPA was added during degradation, the paracetamol degradation efficiency was inhibited to a moderate extent. The results indicate that ·O_2^-, h$^+$ and ·OH are the active species and play important roles in the photocatalytic process.

To further verify the existence of ·OH and ·O_2^- directly, electron paramagnetic resonance (EPR) measurements were carried out on a Bruker EMX spectrometer (Germany). 5, 5-Dimethyl-1-pyrroline N-oxide (DMPO) was used as spin-trapping agent. The sample for EPR measurement was prepared by adding the photocatalyst to DMPO solution with aqueous dispersion for DMPO-·OH and methanol dispersion for DMPO-·O_2^-. The photocatalyst was irradiated with the aforementioned simulated solar light for 10 min. The EPR measurement was conducted within 10 min after illumination. It can be obviously seen from Fig. 8b that the four characteristic peaks of DMPO-·OH adduct with 1:2:2:1 were detected after the aqueous solution of ZnFe-CLDH/RGO was irradiated under simulated solar light [47]. As shown in Fig. 8c, the DMPO-·O_2^- adduct was also detected successfully in the methanol dispersion of the sample and the six characteristic peaks of

the DMPO-·O_2^- adduct were observed under 10 min simulated solar light irradiation [48]. However, the peaks signal of DMPO-·O_2^- is weak. It should be attributed to the relatively short life (a half-life less than 1 min) of DMPO-·O_2^- adduct [49]. In the dark time, no EPR peaks of both DMPO-·OH adduct and DMPO-·O_2^- adduct were found. The EPR results directly confirm that ·OH and ·O_2^- are generated on the surface of ZnFe-CLDH/RGO under simulated solar light irradiation.

3.3. Photocatalytic oxidation-adsorption of As(III)

The adsorption experiments of As(III) and As(V) were carried out in the dark (Fig. 9a). The ZnFe-CLDH/RGO30 displays a higher As(V) adsorption efficiency as compared to As(III) adsorption. It can be ascribed to the arsenic speciation and the composite surface charge. As (III) is mainly present as neutral H_3AsO_3 in a wide pH range from 1 to 9 and as AsO_2^- species at pH higher than 9, while As(V) is mainly present as anionic species $H_2AsO_4^-$ in the pH from 3 to 7 and as $HAsO_4^{2-}$ in the pH range from 7 to 12. In the present study, the pH of reaction systems of both As(III) and As(V) are 7 ± 0.5. As a result, As(III) is present as neutral H_3AsO_3 and As(V) is present as anionic species in our research. Because the pH$_{pzc}$ of the ZnFe-CLDH/RGO30 composite is 7.8 (Fig. 2d), the composite surface is positively charged for pH < 7.8. The ZnFe-CLDH/RGO30 could capture As(V) anions through electrostatic attraction. Therefore, the higher As(V) adsorption efficiency observed in comparison to As(III) can be explained in terms of electrostatic attractions between the As(V) species and the positively charged composite surface. In addition to electrostatic attraction, the removal of arsenic via the formation of monodentate and bidentate complexes is
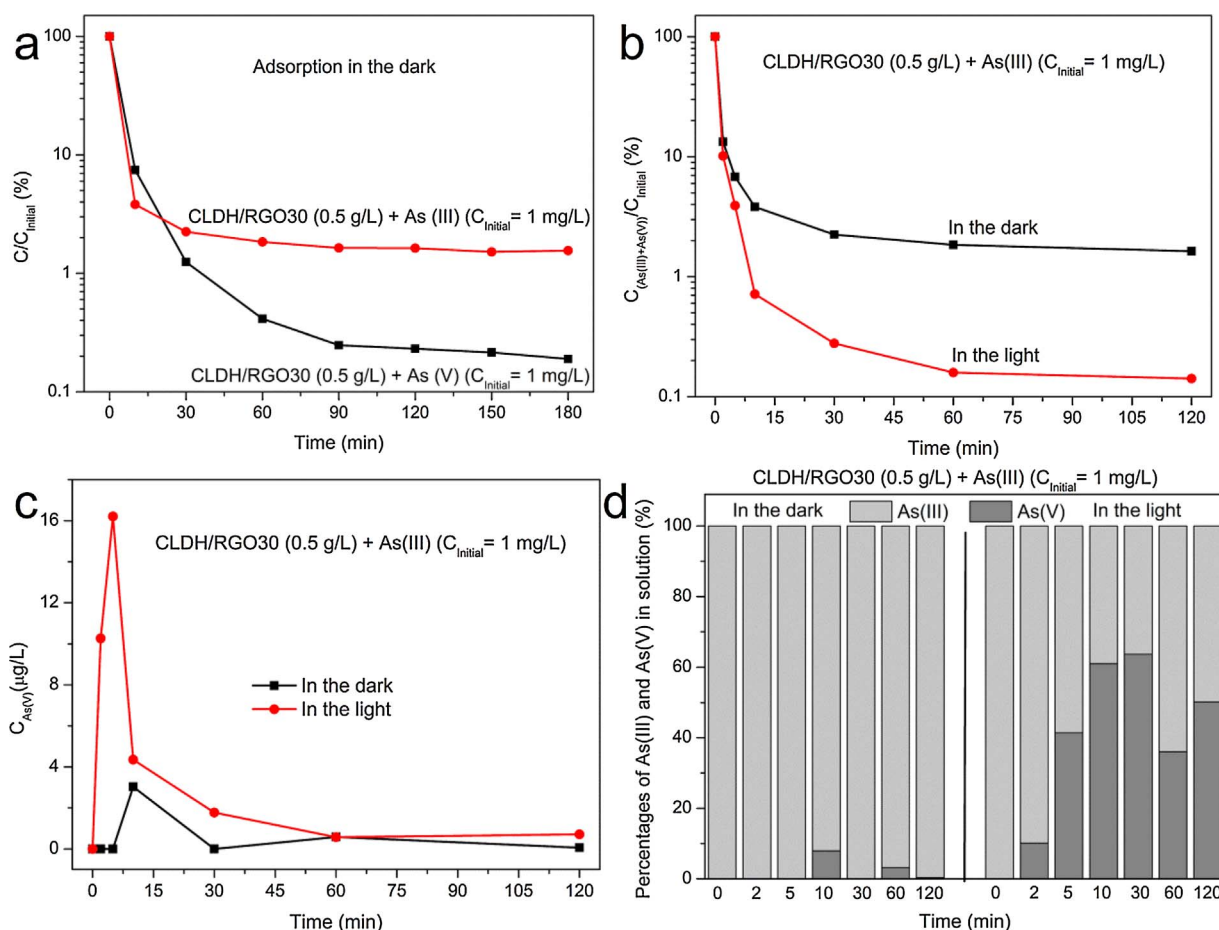
Fig. 9. (a) Time profiles of As(III) and As(V) removal by ZnFe-CLDH/RGO30 in the dark; (b) Time profiles of As removal by ZnFe-CLDH/RGO30 in the dark/light conditions; (c) Residual As(V) concentration in solution in the dark/light conditions; (d) Percentages of residual As(III) and As(V) in solution in the dark/light conditions.
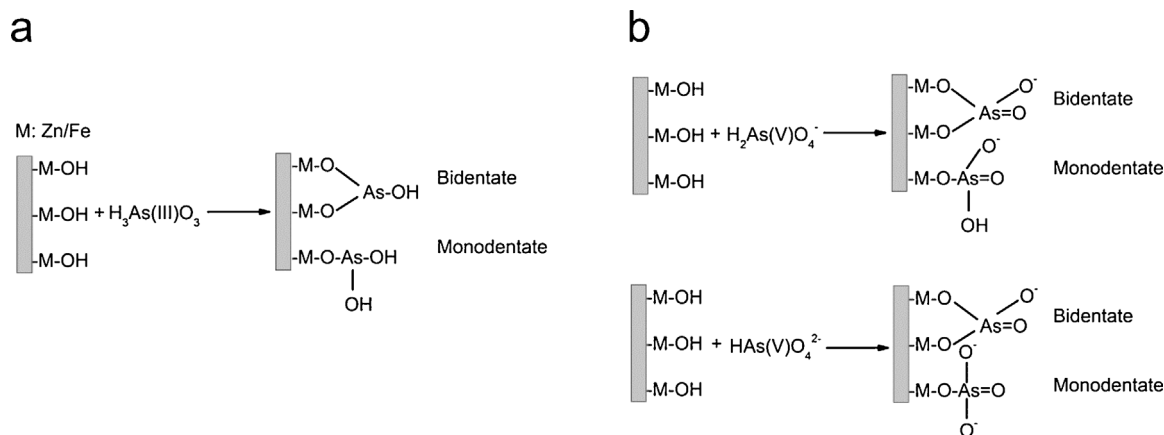

Fig. 10. Schematic diagram for the possible complexes of As(III) (a) and As(V) (b) formed on the ZnFe-CLDH/RGO (M represents Zn/Fe).

also an important way (the possible mechanism is shown in Fig. 10). Thus, for adsorption of As(III), complexation by hydroxyl groups of ZnFe-CLDH/RGO is the dominant mechanism (see Fig. 10a).

The photocatalytic oxidation-adsorption experiment of As(III) was conducted under light irradiation. As shown in Fig. 9b, the ZnFe-CLDH/RGO30 composite displays obviously better As(III) removal efficiency in the light than in the dark. The removal efficiency of total arsenic is more than 99% in just 10 min under light irradiation, which suggests that ZnFe-CLDH/RGO30 possesses a good photocatalytic oxidation-adsorption capability for As(III). Fig. 9c displays the time profiles of residual As(III) and As(V) concentrations in solution in the dark and

light conditions. It can be observed that the As(V) concentration in the light condition sharply increases from 0 to 16.2 µg/L in the first 5 min and then decreases and remains stable at a very low level. The As(V) concentration in solution could be attributed to the combination impacts from both the photocatalytic oxidation of As(III) to less toxic As(V) and the accompanying As(V) adsorption. The photocatalytic oxidation of As(III) leads to increase As(V) concentration in solution, while the adsorption of As(V) reduces the concentration of As(V). The As(V) concentration in solution in the dark condition is obviously lower as compared with that in the light, because As(III) could not be oxidized in the dark. As can be seen from Fig. 9d that the percentage of residual As
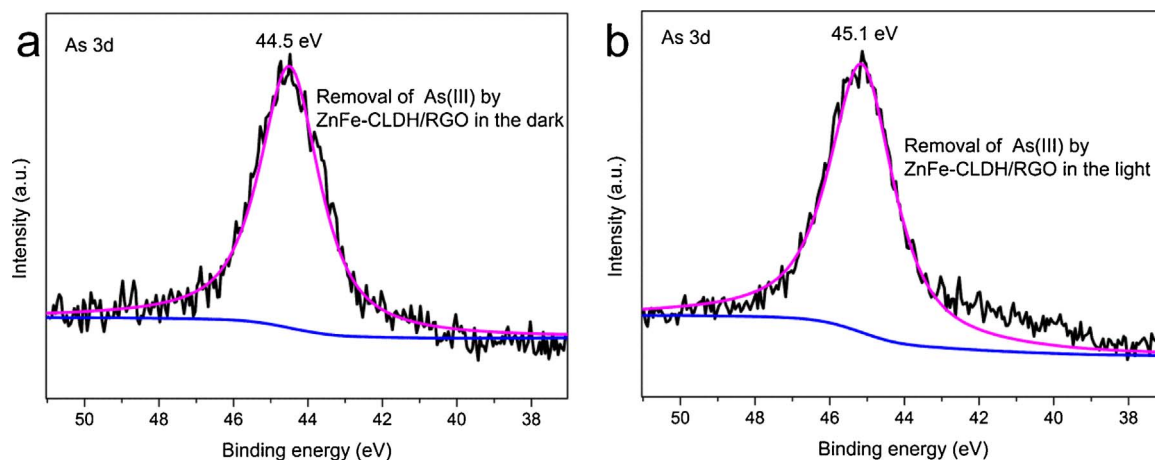
Fig. 11. As 3d XPS spectra on the surface of ZnFe-CLDH/RGO30 after adsorption of As(III) in the dark (a)/light (b) conditions.
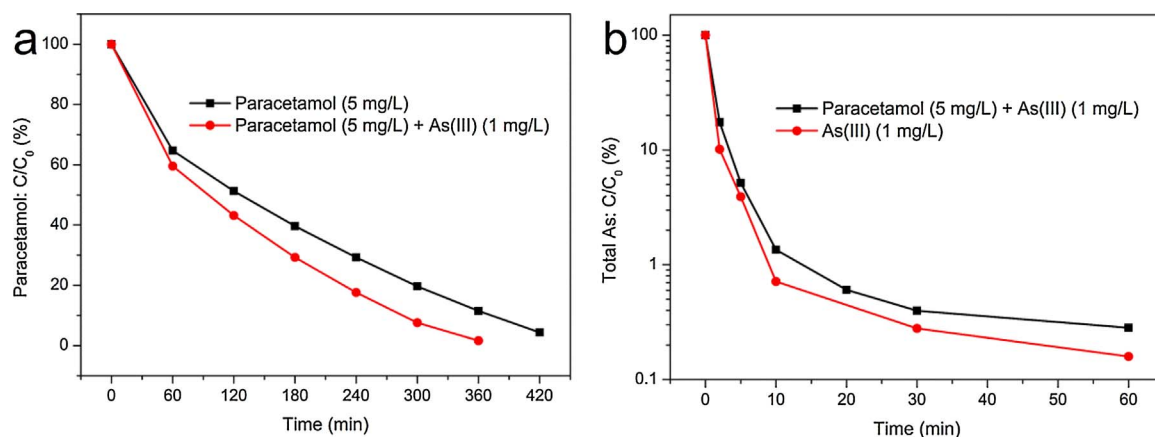

Fig. 12. The removal of paracetamol (a) and arsenic (b) by ZnFe-CLDH/RGO30 in the single system and in the binary system.
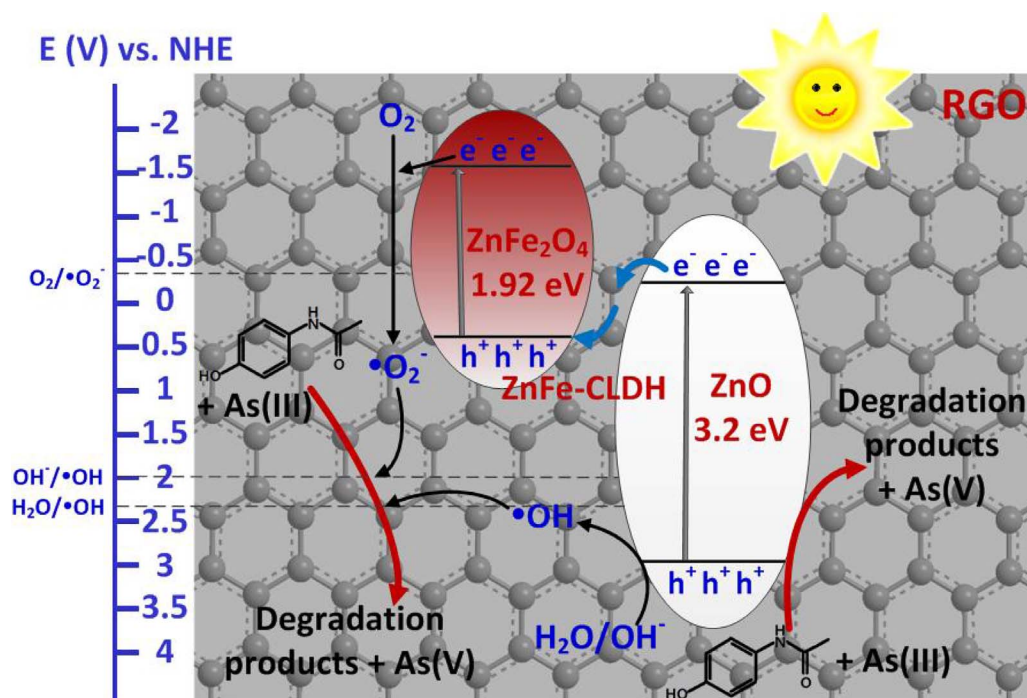

Fig. 13. The proposed photocatalytic mechanism for photocatalytic degradation of paracetamol and photocatalytic oxidation of As(III) over ZnFe-CLDH/RGO under simulated solar light irradiation.
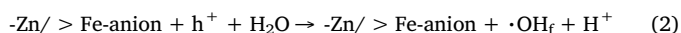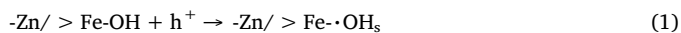
(V) in solution in the light condition is significantly higher than that in the dark. The percentage of residual As(V) in solution is even up to 63.7%. The results further confirm that As(III) can be oxidized to As(V) in the presence of ZnFe-CLDH/RGO under light irradiation.

In order to further investigate the process of As(III) photocatalytic oxidation-adsorption, the XPS was used to analysis the valence state of As on the surface of ZnFe-CLDH/RGO30 after adsorption of As(III) in the dark/light conditions. As shown in Fig. 11, the peaks of As 3d located at 44.5 eV and 45.1 eV can be assigned to As(III) and As(V), respectively [50,51]. The results indicates that arsenic exists in the form of As(III) on the surface of ZnFe-CLDH/RGO30 after reaction in the dark and the arsenic species adsorbed onto the ZnFe-CLDH/RGO30 is As(V) with light irradiation. It proves that the As(III) existed on the surface of ZnFe-CLDH/RGO can be entirely oxidized to less toxic As(V) by the photocatalytic oxidation process.

Taken these together, the ZnFe-CLDH/RGO composite exhibits better As(III) removal efficiency under light irradiation should be attributed to the synergy of the photocatalysis and adsorption.

3.4. Simultaneous removal of paracetamol and As(III)

The experiments of simultaneous removal of paracetamol and As(III) were performed under light irradiation. Fig. 12a shows the photocatalytic degradation of paracetamol in a suspension of ZnFe-CLDH/RGO30 with or without As(III). The degradation of paracetamol is improved in the presence of As(III). This positive effect of As(III) on paracetamol degradation may be ascribed to the following reasons. Anionic As(V) generated from the photocatalytic oxidation of neutral As(III) can be adsorbed on the surface of ZnFe-CLDH/RGO30 through complexation. In such a case, the adsorption of As(V) anions should deplete the surface OH groups of ZnFe-CLDH/RGO30 and increase the density of -Zn/ > Fe-anion (see Fig. 10b). This transformation favors the formation of free ·OH (·OH$_f$) that is more reactive than surface-bound ·OH (·OH$_s$) towards pollutants, because the substitution of surface OH groups by As(V) anions inhibits the reaction between h$^+$ and surface OH groups (generation of ·OH$_s$, reaction 1), but enhances the reaction between h$^+$ and water molecules (generation of ·OH$_f$, reaction 2) [51].

$$-Zn/ > Fe\text{-}OH + h^+ \rightarrow -Zn/ > Fe\text{-·}OH_s \quad (1)$$

$$-Zn/ > Fe\text{-anion} + h^+ + H_2O \rightarrow -Zn/ > Fe\text{-anion} + ·OH_f + H^+ \quad (2)$$

It should be noted that ·OH$_f$ radicals are more reactive than ·OH$_s$ radicals toward pollutants, which are only slightly adsorbed on the ZnFe-CLDH/RGO30 surface, because ·OH$_s$ can only react with substrate near the surface whereas ·OH$_f$ can diffuse out from the surface and react with substrate in the bulk solution. Therefore, the degradation of paracetamol can be improved through the generation of ·OH$_f$ by the adsorption of As(V) anions on the surface of ZnFe-CLDH/RGO30. This study suggests that the degradation of paracetamol in the mixed system of paracetamol/As(III) is more efficient than that in the single system of paracetamol.

Fig. 12b shows the effect of paracetamol on photocatalytic oxidation-adsorption of As(III). The removal efficiency of total As slightly decreases in the presence of paracetamol compared with in the absence of paracetamol. The phenomenon should be attributed to the competition reaction with radicals between As(III) and paracetamol. The removal efficiency of total As reached 99% within 10 min in the single system of As(III) under light irradiation, while it reached 99% within 20 min in the mixed system of paracetamol/As(III), which are below the limit of 10 μg/L set by the World Health Organization.

3.5. Photocatalytic mechanism

On the basis of all above experimental results, the possible photocatalytic mechanism for photocatalytic degradation of paracetamol and

photocatalytic oxidation of As(III) by ZnFe-CLDH/RGO is proposed. The proposed Z-scheme mechanism is shown in Fig. 13.

When the ZnFe-CLDH/RGO is illuminated, both ZnO and ZnFe$_2$O$_4$ can be excited and generate electrons (e$^-$) and holes (h$^+$). According to the Z-scheme mechanism (Fig. 13), the photogenarated electrons and holes are accumulated in the conduction band (CB) of ZnFe$_2$O$_4$ and the valence band (VB) of ZnO, respectively. The presence of RGO, as an electron mediator, could increase the charge separation efficiency [52], and the photogenarated electrons in the CB of ZnO can effectively migrate to the VB of ZnFe$_2$O$_4$ via the RGO, resulting in enhanced photocatalytic activity of the ZnFe-CLDH/RGO system. Since the CB of ZnFe$_2$O$_4$ is more negative than the redox potential of O$_2$/·O$_2^-$ [53,54], the photogenerated electrons in the CB of ZnFe$_2$O$_4$ can react with the O$_2$ and generate ·O$_2^-$, which is responsible for the degradation of paracetamol and oxidation of As(III). Meanwhile, the photogenerated holes in the VB of ZnO can directly oxidize paracetamol and As(III). Besides, the photogenerated holes in the VB of ZnO with a more positive redox potential than that of H$_2$O/·OH and OH$^-$/·OH can also oxidize H$_2$O/OH$^-$ to yield ·OH with high activity for the degradation of paracetamol and oxidation of As(III) in the aqueous solution [54,55]. Such a Z-scheme mechanism can reasonably explain the experimental results in this work.

4. Conclusions

We have successfully synthesized several ZnFe-CLDH/RGO composites by using a hydrothermal-calcination method. The ZnFe-CLDH/RGO composites exhibit remarkably improved photocatalytic performance toward degradation of paracetamol as compared to pristine ZnFe-CLDH. The photocatalytic activity of the screened ZnFe-CLDH/RGO30 for paracetamol degradation is about 3.5 times that of the pristine ZnFe-CLDH. The improved photocatalytic activity could be attributed to the RGO, which could lead to increased pollutant adsorption capacity and enhanced charge separation efficiency. The composite exhibits excellent stability and reusability as a promising photocatalyst for water purification. The ZnFe-CLDH/RGO composite displays better As(III) removal efficiency in the light than in the dark. It could be ascribed to the synergy of photocatalytic oxidation of As(III) to less toxic As(V) and the accompanying arsenic adsorption. Interestingly, our study suggests that the degradation of paracetamol in the mixed system of paracetamol/As(III) is more efficient than that in the single system of paracetamol. Meanwhile, arsenic can be also efficiently removed from the mixed system of paracetamol/As(III). Moreover, the ZnFe-CLDH/RGO suspended in aqueous solution can be easily separated and recovered by an external magnet. This work provides a promising composite for the efficient simultaneous elimination of water environmental inorganic anions and organic pollutants.

References

[1] Y. Kim, K. Choi, J. Jung, S. Park, P.-G. Kim, J. Park, Aquatic toxicity of acetaminophen, carbamazepine, cimetidine, diltiazem and six major sulfonamides, and their potential ecological risks in Korea, Environ. Int. 33 (2007) 370–375.
[2] M. Gonzalez-Pleiter, S. Gonzalo, I. Rodea-Palomares, F. Leganes, R. Rosal, K. Boltes, E. Marco, F. Fernandez-Pinas, Toxicity of five antibiotics and their mixtures towards photosynthetic aquatic organisms: implications for environmental risk assessment, Water Res. 47 (2013) 2050–2064.
[3] T.K. Choueiri, Y. Je, E. Cho, Analgesic use and the risk of kidney cancer: a meta-analysis of epidemiologic studies, Int. J. Cancer 134 (2014) 384–396.
[4] U.S. Food and Drug Administration, FDA Recommends Health Care Professionals Discontinue Prescribing and Dispensing Prescription Combination Drug Products with More than 325 mg of Acetaminophen to Protect Consumers, (2014) (Accessed

14 January 2014), https://www.fda.gov/Drugs/DrugSafety/ucm381644. htm.

[5] S. Eyers, M. Weatherall, S. Jefferies, R. Beasley, Paracetamol in pregnancy and the risk of wheezing in offspring: a systematic review and meta-analysis, Clin. Exp. Allergy 41 (2011) 482–489.

[6] N. Zhang, C. Wei, L. Yang, Occurrence of arsenic in two large shallow freshwater lakes in China and a comparison to other lakes around the world, Microchem. J. 110 (2013) 169–177.

[7] G. Lu, X. Yang, Z. Li, H. Zhao, C. Wang, Contamination by metals and pharmaceuticals in northern Taihu Lake (China) and its relation to integrated biomarker response in fish, Ecotoxicology 22 (2013) 50–59.

[8] Y. Wei, Y. Zhang, J. Xu, C. Guo, L. Li, W. Fan, Simultaneous quantification of several classes of antibiotics in water, sediments, and fish muscles by liquid chromatography-tandem mass spectrometry, Front. Environ. Sci. Eng. 8 (2014) 357–371.

[9] F. Yang, D. Geng, C. Wei, H. Ji, H. Xu, Distribution of arsenic between the particulate and aqueous phases in surface water from three freshwater lakes in China, Environ. Sci. Pollut. Res. 23 (2016) 7452–7461.

[10] Y. Wang, A.N. Ezemaduka, Z. Li, Z. Chen, C. Song, Joint toxicity of arsenic, copper and glyphosate on behavior reproduction and heat shock protein response in caenorhabditis elegans, Bull. Environ. Contam. Toxicol. 98 (2017) 465–471.

[11] G. Cimino-Reale, D. Ferrario, B. Casati, R. Brustio, C. Diodovich, A. Collotta, M. Vahter, L. Gribaldo, Combined in utero and juvenile exposure of mice to arsenate and atrazine in drinking water modulates gene expression and clonogenicity of myeloid progenitors, Toxicol. Lett. 180 (2008) 59–66.

[12] M. Aggarwal, P.B. Wangikar, S.N. Sarkar, G.S. Rao, D. Kumar, P. Dwivedi, J.K. Malik, Effects of low-level arsenic exposure on the developmental toxicity of anilofos in rats, J. Appl. Toxicol. 27 (2007) 255–261.

[13] S. Pausova, J. Krysa, J. Jirkovsky, C. Forano, G. Mailhot, V. Prevot, Insight into the photocatalytic activity of ZnCr-CO3 LDH and derived mixed oxides, Appl. Catal. B Environ. 170 (2015) 25–33.

[14] J. Zhu, Z. Zhu, H. Zhang, H. Lu, Y. Qiu, L. Zhu, S. Kueppers, Enhanced photocatalytic activity of Ce-doped Zn-Al multi-metal oxide composites derived from layered double hydroxide precursors, J. Colloid Interface Sci. 481 (2016) 144–157.

[15] K.M. Parida, L. Mohapatra, Carbonate intercalated Zn/Fe layered double hydroxide: a novel photocatalyst for the enhanced photo degradation of azo dyes, Chem. Eng. J. 179 (2012) 131–139.

[16] C. Gomes Silva, Y. Bouizi, V. Fornes, H. Garcia, Layered double hydroxides as highly efficient photocatalysts for visible light oxygen generation from water, J. Am. Chem. Soc. 131 (2009) 13833–13839.

[17] M. Shao, J. Han, M. Wei, D.G. Evans, X. Duan, The synthesis of hierarchical Zn-Ti layered double hydroxide for efficient visible-light photocatalysis, Chem. Eng. J. 168 (2011) 519–524.

[18] K.-H. Goh, T.-T. Lim, Z. Dong, Application of layered double hydroxides for removal of oxyanions: a review, Water Res. 42 (2008) 1343–1368.

[19] L. Feng, X. Duan, Applications of layered double hydroxides, in: X. Duan, D.G. Evans (Eds.), Layered Double Hydroxides, 2006, pp. 193–223.

[20] F.L. Theiss, S.J. Couperthwaite, G.A. Ayoko, R.L. Frost, A review of the removal of anions and oxyanions of the halogen elements from aqueous solution by layered double hydroxides, J. Colloid Interface Sci. 417 (2014) 356–368.

[21] H. Lu, Z. Zhu, H. Zhang, J. Zhu, Y. Qiu, Simultaneous removal of arsenate and antimonate in simulated and practical water samples by adsorption onto Zn/Fe layered double hydroxide, Chem. Eng. J. 276 (2015) 365–375.

[22] L. Yang, Z. Shahrivari, P.K.T. Liu, M. Sahimi, T.T. Tsotsis, Removal of trace levels of arsenic and selenium from aqueous solutions by calcined and uncalcined layered double hydroxides (LDH), Ind. Eng. Chem. Res. 44 (2005) 6804–6815.

[23] C. Lei, M. Pi, P. Kuang, Y. Guo, F. Zhang, Organic dye removal from aqueous solutions by hierarchical calcined Ni-Fe layered double hydroxide: isotherm, kinetic and mechanism studies, J. Colloid Interface Sci. 496 (2017) 158–166.

[24] J. Hong, Z. Zhu, H. Lu, Y. Qiu, Effect of metal composition in lanthanum-doped ferric-based layered double hydroxides and their calcined products on adsorption of arsenate, RSC Adv. 4 (2014) 5156–5164.

[25] K.I. Bolotin, K.J. Sikes, Z. Jiang, M. Klima, G. Fudenberg, J. Hone, P. Kim, H.L. Stormer, Ultrahigh electron mobility in suspended graphene, Solid State Commun. 146 (2008) 351–355.

[26] Q. Xiang, J. Yu, M. Jaroniec, Graphene-based semiconductor photocatalysts, Chem. Soc. Rev. 41 (2012) 782–796.

[27] M.D. Stoller, S. Park, Y. Zhu, J. An, R.S. Ruoff, Graphene-Based ultracapacitors, Nano Lett. 8 (2008) 3498–3502.

[28] S. Stankovich, D.A. Dikin, G.H.B. Dommett, K.M. Kohlhaas, E.J. Zimney, E.A. Stach, R.D. Piner, S.T. Nguyen, R.S. Ruoff, Graphene-based composite materials, Nature 442 (2006) 282–286.

[29] H. Moussa, E. Girot, K. Mozet, H. Alem, G. Medjandi, R. Schneider, ZnO rods/reduced graphene oxide composites prepared via a solvothermal reaction for efficient sunlight-driven photocatalysis, Appl. Catal. B Environ. 185 (2016) 11–21.

[30] H. Adamu, P. Dubey, J.A. Anderson, Probing the role of thermally reduced graphene oxide in enhancing performance of TiO2 in photocatalytic phenol removal from aqueous environments, Chem. Eng. J. 284 (2016) 380–388.

[31] M. Ahmad, E. Ahmed, Z.L. Hong, J.F. Xu, N.R. Khalid, A. Elhissi, W. Ahmed, A facile one-step approach to synthesizing ZnO/graphene composites for enhanced degradation of methylene blue under visible light, Appl. Surf. Sci. 274 (2013) 273–281.

[32] Z. Chen, N. Zhang, Y.-J. Xu, Synthesis of graphene-ZnO nanorod nanocomposites with improved photoactivity and anti-photocorrosion, CrystEngComm 15 (2013) 3022–3030.

[33] X. Zeng, Z. Wang, G. Wang, T.R. Gengenbach, D.T. McCarthy, A. Deletic, J. Yu, X. Zhang, Highly dispersed TiO2 nanocrystals and WO3 nanorods on reduced graphene oxide: z-scheme photocatalysis system for accelerated photocatalytic water disinfection, Appl. Catal. B-Environ. 218 (2017) 163–173.

[34] Y. Shao, J. Wang, M. Engelhard, C. Wang, Y. Lin, Facile and controllable electrochemical reduction of graphene oxide and its applications, J. Mater. Chem. 20 (2010) 743–748.

[35] N.B.-H. Abdelkader, A. Bentouami, Z. Derriche, N. Bettahar, L.C. de Menorval, Synthesis and characterization of Mg-Fe layer double hydroxides and its application on adsorption of Orange G from aqueous solution, Chem. Eng. J. 169 (2011) 231–238.

[36] Y. Yoon, W.K. Park, T.-M. Hwang, D.H. Yoon, W.S. Yang, J.-W. Kang, Comparative evaluation of magnetite-graphene oxide and magnetite-reduced graphene oxide composite for As(III) and As(V) removal, J. Hazard. Mater. 304 (2016) 196–204.

[37] R. Karthik, J.V. Kumar, S.-M. Chen, C. Karuppiah, Y.-H. Cheng, V. Muthuraj, A study of electrocatalytic and photocatalytic activity of cerium molybdate nanocubes decorated graphene oxide for the sensing and degradation of antibiotic drug chloramphenicol, ACS Appl. Mater. Interfaces 9 (2017) 6547–6559.

[38] Z. Chang, D.G. Evans, X. Duan, C. Vial, J. Ghanbaja, V. Prevot, M. de Roy, C. Forano, Synthesis of Zn-Al-CO3 layered double hydroxides by a coprecipitation method under steady-state conditions, J. Solid State Chem. 178 (2005) 2766–2777.

[39] M. Kim, C. Lee, J. Jang, Fabrication of highly flexible, scalable, and HighPerformance supercapacitors using Polyaniline/Reduced graphene oxide film with enhanced electrical conductivity and crystallinity, Adv. Funct. Mater. 24 (2014) 2489–2499.

[40] S. Bag, K. Roy, C.S. Gopinath, C.R. Raj, Facile single-Step synthesis of nitrogen-Doped reduced graphene oxide-Mn3O4 hybrid functional material for the electrocatalytic reduction of oxygen, ACS Appl. Mater. Interfaces 6 (2014) 2692–2699.

[41] J. Shen, M. Shi, B. Yan, H. Ma, N. Li, M. Ye, One-pot hydrothermal synthesis of Ag-reduced graphene oxide composite with ionic liquid, J. Mater. Chem. 21 (2011) 7795–7801.

[42] J. Wang, Y. Hernandez, M. Lotya, J.N. Coleman, W.J. Blau, Broadband nonlinear optical response of graphene dispersions, Adv. Mater. 21 (2009) 2430–2435.

[43] J. Liu, Z. Yin, X. Cao, F. Zhao, L. Wang, W. Huang, H. Zhang, Fabrication of flexible, all-Reduced graphene oxide non-Volatile memory devices, Adv. Mater. 25 (2013) 233–238.

[44] W. Ai, Z. Luo, J. Jiang, J. Zhu, Z. Du, Z. Fan, L. Xie, H. Zhang, W. Huang, T. Yu, Nitrogen and sulfur codoped graphene: multifunctional electrode materials for high-Performance Li-Ion batteries and oxygen reduction reaction, Adv. Mater. 26 (2014) 6186- + .

[45] F. Zou, X. Hu, Z. Li, L. Qie, C. Hu, R. Zeng, Y. Jiang, Y. Huang, MOF-Derived porous ZnO/ZnFe2O4/C octahedra with hollow interiors for high-Rate lithium-Ion batteries, Adv. Mater. 26 (2014) 6622–6628.

[46] F. Chen, Q. Yang, X. Li, G. Zeng, D. Wang, C. Niu, J. Zhao, H. An, T. Xie, Y. Deng, Hierarchical assembly of graphene-bridged Ag3PO4/Ag/BiVO4 (040) Z-scheme photocatalyst: an efficient, sustainable and heterogeneous catalyst with enhanced visible-light photoactivity towards tetracycline degradation under visible light irradiation, Appl. Catal. B-Environ. 200 (2017) 330–342.

[47] Q. Peng, H. Zhao, L. Qian, Y. Wang, G. Zhao, Design of a neutral photo-electro-Fenton system with 3D-ordered macroporous Fe2O3/carbon aerogel cathode: high activity and low energy consumption, Appl. Catal. B-Environ. 174 (2015) 157–166.

[48] W. Wang, T.W. Ng, W.K. Ho, J. Huang, S. Liang, T. An, G. Li, J.C. Yu, P.K. Wong, CdIn2S4 microsphere as an efficient visible-light-driven photocatalyst for bacterial inactivation: synthesis, characterizations and photocatalytic inactivation mechanisms, Appl. Catal. B-Environ. 129 (2013) 482–490.

[49] T. Ando, Y. Yonamoto, In situ EPR detection of reactive oxygen species in adherent cells using polylysine-Coated glass plate, Appl. Magn. Reson. 46 (2015) 977–986.

[50] J. Hu, S. Weng, Z. Zheng, Z. Pei, M. Huang, P. Liu, Solvents mediated-synthesis of BiOI photocatalysts with tunable morphologies and their visible-light driven photocatalytic performances in removing of arsenic from water, J. Hazard. Mater. 264 (2014) 293–302.

[51] J. Kim, J. Kim, Arsenite oxidation-enhanced photocatalytic degradation of phenolic pollutants on platinized TiO2, Environ. Sci. Technol. 48 (2014) 13384–13391.

[52] A. Iwase, Y.H. Ng, Y. Ishiguro, A. Kudo, R. Amal, Reduced graphene oxide as a solid-State electron mediator in Z-Scheme photocatalytic water splitting under visible light, J. Am. Chem. Soc. 133 (2011) 11054–11057.

[53] S. Zhang, J. Li, M. Zeng, G. Zhao, J. Xu, W. Hu, X. Wang, In situ synthesis of water-Soluble magnetic graphitic carbon nitride photocatalyst and its synergistic catalytic performance, ACS Appl. Mater. Interfaces 5 (2013) 12735–12743.

[54] X. She, J. Wu, H. Xu, J. Zhong, Y. Wang, Y. Song, K. Nie, Y. Liu, Y. Yang, M.-T.F. Rodrigues, R. Vajtai, J. Lou, D. Du, H. Li, P.M. Ajayan, High efficiency photocatalytic water splitting using 2D alpha-Fe2O3/g-C3N4 Z-Scheme catalysts, Adv. Energy Mater. 7 (2017).

[55] W. He, H.-K. Kim, W.G. Warner, D. Melka, J.H. Callahan, J.-J. Yin, Photogenerated charge carriers and reactive oxygen species in ZnO/Au hybrid nanostructures with enhanced photocatalytic and antibacterial activity, J. Am. Chem. Soc. 136 (2014) 750–757.